ACS APPLIED MATERIALS & INTERFACES

www.acsami.org

Research Article

Enhancing Ferromagnetism and Tuning Electronic Properties of CrI_3 Monolayers by Adsorption of Transition-Metal Atoms

Qiang Yang, Xiaohui Hu,* Xiaodong Shen, Arkady V. Krasheninnikov, Zhongfang Chen, and Litao Sun

Cite This: *ACS Appl. Mater. Interfaces* 2021, 13, 21593−21601

Read Online

ACCESS | Metrics & More | Article Recommendations | Supporting Information

ABSTRACT: Among first experimentally discovered two-dimensional (2D) ferromagnetic materials, chromium triiodide (CrI_3) monolayers have attracted particular attention due to their potential applications in electronics and spintronics. However, the Curie temperature T_c of the CrI_3 monolayer is below room temperature, which greatly limits practical development of the devices. Herein, using density functional theory calculation, we explore how the electronic and magnetic properties of CrI_3 monolayers change upon adsorption of 3d transition-metal (TM) atoms (from Sc to Zn). Our results indicate that the electronic properties of the TM−CrI_3 system can be tuned from semiconductor to metal/half-metal/spin gapless semiconductor depending on the choice of the adsorbed TM atoms. Moreover, the adsorption can improve the ferromagnetic stability of CrI_3 monolayers by increasing both magnetic moments and T_c. Notably, T_c of CrI_3 with Sc and V adatoms can be increased by nearly a factor of 3. We suggest postsynthesis doping of 2D CrI_3 by deposition of TM atoms as a new route toward potential applications of TM−CrI_3 systems in nanoelectronic and spintronic devices.

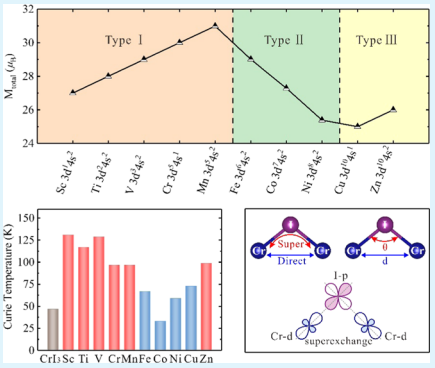

KEYWORDS: *CrI_3 monolayer, transition-metal adsorption, electronic properties, ferromagnetism, magnetic properties*

INTRODUCTION

Two-dimensional (2D) materials have been shown to possess unique and fascinating physicochemical properties pointing to their potential applications in electronics.[1−8] Unfortunately, most of these 2D materials such as graphene, boron nitride, and transition-metal dichalcogenides are nonmagnetic, which represents a significant obstacle for applications of 2D materials in spintronic devices. Hence, substantial research effort has been made to introduce magnetism in these nonmagnetic systems, such as doping,[9−11] defect,[12−14] and strain engineering,[15,16] as well as the proximity effect.[17] However, although local magnetic moments have been successfully introduced by these methods, the formation of a macroscopic state remains a big challenge. The other way to achieve 2D spintronic materials is to develop 2D materials with intrinsic ferromagnetic ordering. In 2017, the existence of the long-ranged ferromagnetic order was demonstrated in 2D CrI_3[18] and $Cr_2Ge_2Te_6$[19] with spins being oriented perpendicular to the material plane in the former and with arbitrary directions of spins in the latter system. After that, some other 2D ferromagnetic materials have been successfully prepared and studied, such as Fe_3GeTe_2 and $CrBr_3$.[20−23] Besides, several 2D ferromagnetic materials have been theoretically predicted, such as CrX (X = P, As),[24] GdI_2,[25] and FeB_3,[26] but not synthesized yet. These findings not only opened new avenues for the fundamental research on magnetism in systems with a reduced dimensionality but also provided exciting new opportunities for 2D spintronics.

As one of the first experimentally discovered 2D ferromagnetic materials, the CrI_3 monolayer has attracted especially much attention. Due to its intrinsic ferromagnetism, strong perpendicular magnetic anisotropy, giant magneto band-structure effect, distinct spin−lattice and spin−phonon coupling, and robust topological properties,[27−32] CrI_3 monolayer can be a potential candidate for spintronic devices. However, its Curie temperature T_c (only 45 K)[18] is much lower than room temperature, which greatly limits its practical applications. Therefore, a crucial issue is how to adjust the magnetic properties of CrI_3 and improve its ferromagnetic stability. Several approaches have been suggested to enhance the ferromagnetism of CrI_3, including electrostatic doping, electric field, defect engineering, strain, etc.[33−39] For example, the characteristics such as saturation magnetization, coercive force, and Curie temperature of the CrI_3 monolayer can be improved by electrostatic doping.[33] By applying an external electric field, magnetism in the CrI_3 bilayer can be further controlled.[35] It was predicted that surface iodine vacancies not only enhance the intrinsic ferromagnetism of the CrI_3 monolayer but also induce switchable electric polarization.[36]

Received: January 31, 2021
Accepted: April 15, 2021
Published: April 27, 2021

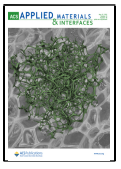

https://doi.org/10.1021/acsami.1c01701
ACS Appl. Mater. Interfaces 2021, 13, 21593−21601

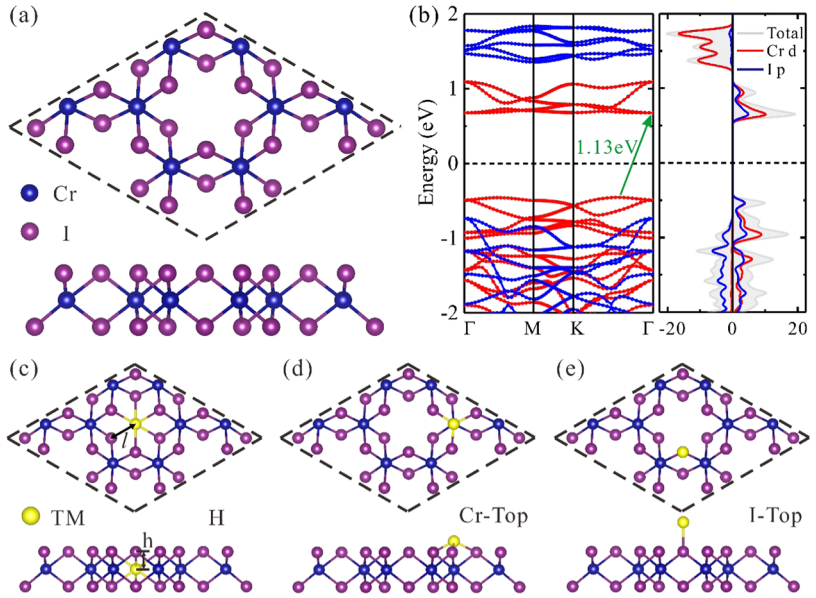

Figure 1. (a) Top and side views of the crystalline structure of the CrI_3 monolayer. (b) Spin-polarized band structure and partial density of states (PDOS) of the CrI_3 monolayer. The red and blue dotted lines denote spin-up and spin-down channels, respectively. The Fermi level is indicated by the black dashed lines. The top and side views of the crystalline structure of the system with TM atoms adsorbed in three different positions denoted as (c) H, (d) Cr-Top, and (e) I-Top. The blue, purple, and yellow balls represent Cr, I, and TM atoms, respectively.

First-principles calculations also indicated that the magnetic anisotropy energy of the CrI_3 monolayer can be increased by 47% under a 5% compressive strain.[40]

Doping is one of the most commonly used methods to tailor the electronic and magnetic properties of 2D materials.[41−43] The robust ferromagnetism was observed in Mn-doped MoS_2 synthesized by a hydrothermal method,[44] and induced magnetism was found in Re-doped $MoSe_2$ monolayer.[45] Recent theoretical studies also indicated that N doping in ReS_2 can induce the transition from nonmagnetic to tunable magnetic state.[46] Recent experimental results suggest that V-doped $MoTe_2$ is a room-temperature ferromagnetic semiconductor.[9] Alkali-metal adsorption dramatically increased the magnetic anisotropy energy of the $Cr_2Ge_2Te_6$ monolayer, leading to a significant increase in the Curie temperature.[47] The adsorption of Li atoms can enhance the ferromagnetism of CrI_3 by increasing both the magnetic moment and the Curie temperature.[48]

In this work, by means of systematic density functional theory (DFT) calculation, we investigate another way to improve the magnetic characteristics of CrI_3. Specifically, we study the influence of 3d transition-metal (TM) atoms (from Sc to Zn) adsorption on the electronic and magnetic properties of the CrI_3 monolayer. We demonstrate that electronic properties can be varied in a wide range depending on the TM atoms adsorbed on the CrI_3 monolayer. In addition, ferromagnetism in the CrI_3 monolayer can be remarkably enhanced by adsorption of TM atoms, which can be ascribed to the interplay between direct exchange and superexchange interactions. Our findings provide a promising pathway to tune the electronic properties and improve ferromagnetism in CrI_3 monolayers, which would make this material one step closer to the potential applications in nanoelectronic and spintronic devices.

COMPUTATIONAL METHOD

Our DFT calculations were carried out using the projector-augmented wave (PAW) method[49,50] implemented in Vienna Ab initio Simulation Package (VASP).[51,52] The exchange interaction and correlations were described by the generalized-gradient approximation (GGA) with the Perdew−Burke−Ernzerhof (PBE)[53] parametrization. An energy cutoff of 500 eV was set for the plane-wave basis. The Brillouin zone *k*-point sampling of 7 × 7 × 1 grid mesh was used for geometry optimizations. The lattice constants and atomic positions were fully relaxed until the total energy and force were less than 10^{-6} eV and 0.01 eV/Å, respectively. A vacuum region of at least 18 Å along the out-of-plane direction was introduced to avoid interaction between periodic images of the system. The results were examined using the PBE + U functional. The Hubbard *U* values are set to be 3.0 and 2.5 eV for Cr and 3d TM atoms,[54−56] respectively. The spin−orbit coupling (SOC) was also included to examine the electronic structures of a pristine CrI_3 monolayer and magnetic moments of TM−CrI_3. Further, the hybrid functional HSE06[57] was adopted to investigate the electronic structures of Sc−CrI_3 and Mn−CrI_3. The Monte Carlo (MC) simulation based on the Ising model[34,55] was used to estimate the Curie temperature of CrI_3 and TM−CrI_3.

RESULTS AND DISCUSSION

The CrI_3 monolayer is an I−Cr−I sandwiched layer structure, where the magnetic Cr^{3+} ions form a honeycomb network in octahedral coordination, edge-sharing with six I^- ions (Figure 1a). The optimized lattice constant of the CrI_3 monolayer is 7.01 Å, the bond length between Cr and I atoms is 2.74 Å, which is in good agreement with previous reports.[48,58] It can be seen from Figure 1b that the CrI_3 monolayer is an indirect semiconductor with a band gap of 1.13 eV;[47] the valence band maximum (VBM) and the conduction band minimum (CBM) are mainly contributed by the Cr 3d and I 5p states. To evaluate the magnetic ground states of the CrI_3 monolayer, four different magnetic configurations are considered: the

https://doi.org/10.1021/acsami.1c01701
ACS Appl. Mater. Interfaces 2021, 13, 21593−21601

ferromagnetic (FM), Néel antiferromagnetic (Néel-AFM), zigzag antiferromagnetic (zigzag-AFM), and stripy antiferromagnetic (stripy-AFM) state, as shown in Figure S1. The calculated total energies show that the FM state is energetically most favorable, indicating that ferromagnetic coupling dominates in the CrI_3 monolayer. The spin-density distribution of the CrI_3 monolayer (Figure S2) indicates that the magnetism mainly originates from magnetic moments localized on Cr atoms (3.09 μ_B per Cr atom), which is consistent with the experimental result (3.1 μ_B per Cr atom).[59] The good agreement suggests that our DFT calculations can correctly describe the geometry and properties of the CrI_3 monolayer. We also calculated the lattice constant, band structure, and magnetic moment of the CrI_3 monolayer using the PBE + U method. As shown in Table S1 and Figure S3, the lattice constant and magnetic moment of the CrI_3 monolayer are consistent with the results calculated by PBE. The PBE + U band gap of the CrI_3 monolayer (1.23 eV) only slightly differs from the PBE gap (1.13 eV). When the SOC is considered, the band gap of the CrI_3 monolayer is reduced to 0.89 eV, which is smaller than that calculated from PBE and PBE + U.

Having analyzed the properties of the pristine CrI_3, we moved on to the investigations of the adsorbed configurations and formation energies of the CrI_3 monolayer upon 3d TM atoms (from Sc to Zn) adsorption. A 2 × 2 × 1 CrI_3 supercell was chosen to represent the system (TM−CrI_3). Three possible adsorption sites of TM atoms on the CrI_3 monolayer were considered: the middle of a hexagon (H), on top of a Cr atom (Cr-Top) and on top of an I atom (I-Top), as shown in Figure 1c−e. The formation energy E_f of TM−CrI_3 is defined as $E_f = E_{CrI_3+TM} - E_{CrI_3} - \mu_{TM}$, where E_{CrI_3+TM} is the total energy of the CrI_3+TM system after structural relaxation, E_{CrI_3} is the total energy of pristine CrI_3, and μ_{TM} is the chemical potential of the TM atom in the isolated TM dimer ($\mu_{TM} = 1/2E_{TM_2}$). According to our definition of formation energy, the more negative value of E_f indicates the higher stability of the adsorption configuration. Our computations showed that E_f values of TM−CrI_3 for the H site are more negative than that for the Cr-Top and I-Top sites (Figure 2a), suggesting that all 3d TM atoms prefer to be adsorbed on the H site. Note that all of the E_f values of TM−CrI_3 for the H site are negative and sizable, which indicates that TM atoms prefer to occupy positions in the atomic network of CrI_3 sheet rather than form dimers and likely bigger clusters. Thus, the formation of TM clusters can be avoided. In addition, the energy of TM atoms from bulk phase was also chosen as a reference to calculate the formation energy. As shown in Figure S4, TM atoms adsorption on the H site is also preferable over the Cr-Top and I-Top sites.

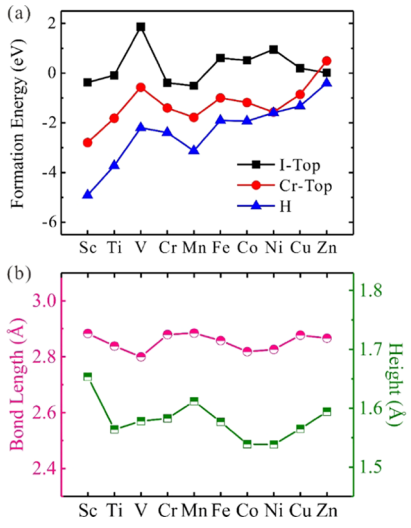

Figure 2. (a) Formation energy of TM atoms adsorbed on H, Cr-Top, and I-Top in the CrI_3 monolayer. (b) Height of TM atoms and length of the bond to nearest I atoms for adsorption on the H site.

Besides evaluating the thermodynamic stability, we also examined the thermal stability of CrI_3 after TM atoms adsorption on the H site by performing DFT-based molecular dynamics (MD) simulation[42] at 300 K. The TM−CrI_3 structures well preserve their original framework after 5 ps (Figure S5), suggesting their thermal stability. Thus, we will focus on the H configuration in the following discussion. For the H configuration, the TM adatom forms covalent bonds with the nearest six I atoms, with the TM−I bond lengths being generally larger than 2.80 Å (see Figure 2b), varying with different TM atoms. The height of TM atoms with regard to the CrI_3 surface is in the range of 1.54−1.65 Å, as shown in Figure 2b. Zn−CrI_3 has the least negative formation energy of −0.41 eV, indicating that Zn atom bonds weakly with the CrI_3 monolayer. Except Zn atom, the E_f values for the other TM atoms are quite large (−1.33 to −4.92 eV), indicating that they bind strongly to the CrI_3 monolayer. Among them, Sc−CrI_3 has the most negative formation energy of −4.92 eV, which can be understood by the fact that the energy of the 3d orbital of Sc is higher than that of other 3d TM atoms.

The spin-polarized band structures of TM atoms adsorbed on CrI_3 monolayer are presented in Figures 3 and S6. It is evident that the adsorption of TM atoms can strongly influence the electronic properties of the CrI_3 monolayer. After Sc adsorption, the metallic behavior is observed in the spin-up channel, while there is a band gap of 1.76 eV in the spin-down channel, as illustrated in Figure 3a. Thus, the Sc−CrI_3 system shows half-metallicity and can provide 100% spin-polarized current. Examining the PDOS revealed that the bands near the Fermi level mainly come from the 3d orbitals of Sc and the neighboring Cr atoms in Sc−CrI_3. Similarly, the half-metal behaviors are also found for Ti, V, Cr, and Zn−CrI_3 (see Figure S6a−c,f). Interestingly, the spin gapless semiconductor (SGS) is expected for the adsorption of Mn atom on the CrI_3 monolayer, i.e., the spin-up channel has a tiny gap of 0.02 eV, while the spin-down channel displays the semiconducting character with a band gap of 1.86 eV, as shown in Figure 3b. According to the definition of Wang and Hu,[42,60] a band gap less than 0.1 eV can be termed as "gapless". Different from the case of Sc−CrI_3, the bands near the Fermi level are dominated by the 3d orbitals of Cr atoms adjacent to the Mn atom in Mn−CrI_3. The SGS is also found in Co−CrI_3 (see Figure S6d). For SGS materials, electrons with a particular spin can easily be excited from the valence band to the conduction band, giving rise to 100% spin-polarized current, which is desirable for the spintronic devices. As for Fe and Ni adsorption, the metallic behavior can be found in the spin-up and spin-down channels (see Figures 3c and S6e), which leads to a semiconductor-to-metal transition in the CrI_3 monolayer. The PDOS analysis suggests that the Fe (Ni) and Cr 3d orbitals are responsible for the metallicity. For the adsorption of Cu, the system preserves the semiconducting character with a band gap of 0.69 eV, significantly decreased as compared to

https://doi.org/10.1021/acsami.1c01701
ACS Appl. Mater. Interfaces 2021, 13, 21593−21601

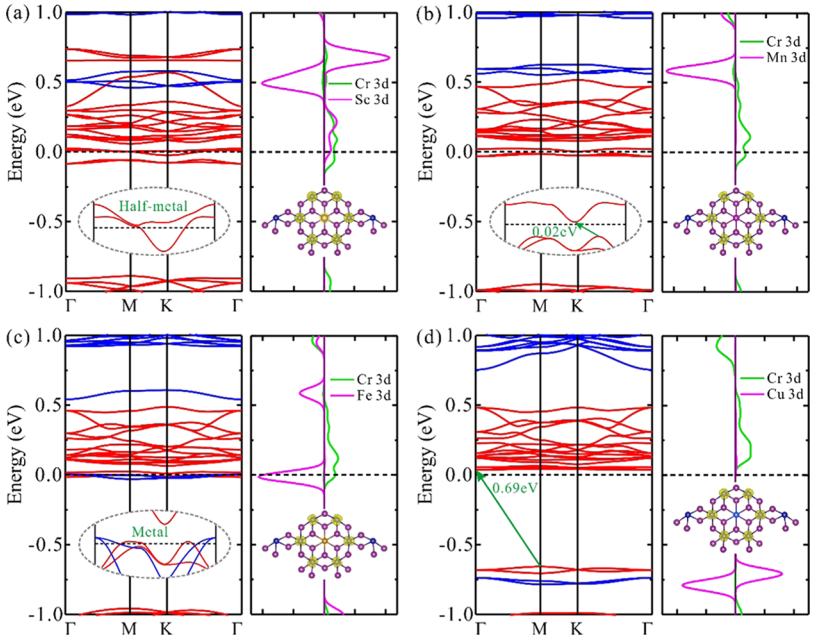

Figure 3. Spin-polarized band structures, partial charge densities, and PDOS of (a) Sc−CrI_3, (b) Mn−CrI_3, (c) Fe−CrI_3, and (d) Cu−CrI_3. The red and blue solid lines indicate spin-up and spin-down channels in the band structures, respectively. The Fermi level is indicated by the black dashed lines. The isosurface is set to be 0.002 e/Å^3.

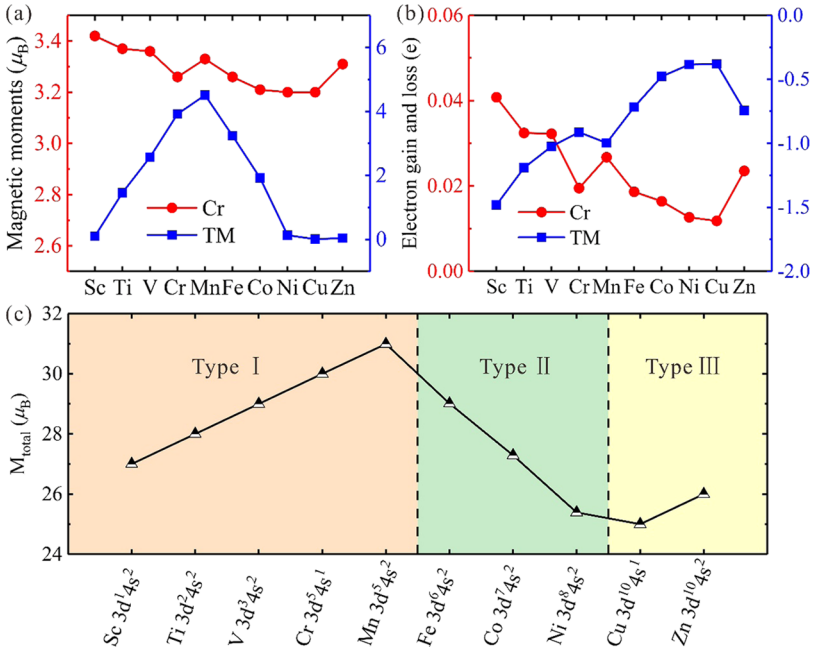

Figure 4. (a) Local magnetic moments of Cr (near the H site) and TM atoms in the CrI_3 monolayer with TM atoms adsorbed on the H site. (b) Charge transfer of Cr and TM atoms in TM−CrI_3. (c) Total magnetic moments of TM−CrI_3 in a 2 × 2 × 1 supercell. The two vertical dashed lines divide the total magnetic moments of TM−CrI_3 into three types.

that of the pristine CrI_3 monolayer (1.13 eV). The VBM and CBM are mainly contributed by the 3d orbitals of Cu atom and Cr atoms, respectively, as shown in Figure 3d. The above PDOS analysis can be further substantiated by the partial charge densities of the bands near the Fermi level in Figure 3.

Taking Sc−CrI_3, Mn−CrI_3, Fe−CrI_3, and Cu−CrI_3 as examples, we examined their band structures using PBE + U functional, as shown in Figure S7. It can be seen that Sc−CrI_3, Mn−CrI_3, and Cu−CrI_3 remain half-metal, the SGS, and semiconducting characters, respectively, while Fe−CrI_3 presents the SGS behavior. Taking into account that the band structures at the Fermi level of half-metal and SGS are sensitive to the choice of the calculation method, the hybrid HSE06 functional was used to check the band structures of Sc−CrI_3 and Mn−CrI_3. As shown in Figure S8, Sc−CrI_3 and Mn−CrI_3 preserve the half-metal and SGS behaviors, respectively.

Next, we explore the effect of TM atoms on the magnetic properties of a CrI_3 monolayer. For simplification, the local magnetic moments of Cr, TM atoms, and the total magnetic

https://doi.org/10.1021/acsami.1c01701
ACS Appl. Mater. Interfaces 2021, 13, 21593−21601

moments of TM−CrI_3 are named as M_{Cr}, M_{TM}, and M_{total}, respectively. As shown in Figure 4a, the M_{Cr} ranges from 3.20 to 3.42 μ_B, larger than that in the pristine CrI_3 monolayer (3.09 μ_B). Among them, Sc−CrI_3 has the largest M_{Cr} of 3.42 μ_B, while Ni−CrI_3 and Cu−CrI_3 have the smallest M_{Cr} of 3.20 μ_B. The M_{Cr} variation with TM atoms can be understood from the charge transfer in TM−CrI_3 (Figure 4b). Specifically, in Sc−CrI_3, each Cr atom has the largest electron gain of about 0.04 e, while in Ni−CrI_3 and Cu−CrI_3, each Cr atom has the least electron gain of 0.01*e*. On the other hand, the local magnetic moments of TM atoms (from Sc to Cu) are 0.10,1.46, 2.57, 3.92, 4.51, 3.24, 1.92, 0.13, and 0.01 μ_B, respectively, smaller than those of the free TM atoms (Table S2). The reduction of the M_{TM} well correlates with the charge transfer from the TM atom to the CrI_3 monolayer (Figure 4b).

To gain further insights into the total magnetic moments of TM−CrI_3, we examined the spin-density distributions (Figure S2). The spin-density distributions show that M_{total} mainly stem from the Cr atoms and partly from the TM atoms in TM−CrI_3. The M_{total} first increases and then decreases with increasing the TM atomic number, which exhibits a "volcano" curve, as shown in Figure 4c. The overall similar trends have also been reported in TM atom-adsorbed graphene, $MoSe_2$, and phosphorene.[10,41,61] The M_{total} of TM−CrI_3 can be divided into three types: type I (TM = Sc, Ti, V, Cr, and Mn), type II (TM = Fe, Co, and Ni), and type III (TM = Cu and Zn). For type I, the M_{total} of TM−CrI_3 is integer and increases linearly from 27 to 31 μ_B (from Sc to Mn) in the 2 × 2 supercell. We note that the M_{total} of TM−CrI_3 (TM = Sc, Ti, V, Cr, and Mn) is related to the number of (s + d) electrons in the outermost electron shell. For example, a Sc atom has three outermost electrons, accordingly M_{total} increases by 3 μ_B with regard to that of the pristine CrI_3 monolayer (24 μ_B). As the number of (s + d) electrons increases from 4 to 7 (Ti to Mn), M_{total} increases stepwise from 28 to 31 μ_B (Ti to Mn). Different from the case of type I, M_{total} of Fe−, Co−, and Ni−CrI_3 is approximately linearly reduced by 2 μ_B as compared to that for earlier TMs. For Cu−CrI_3, the Cu atom possesses 11 outermost electrons, wherein 10 electrons fill all of the 3d orbitals, and the left one gives rise to M_{total} increase by 1 μ_B with regard to that of the pristine CrI_3 monolayer. As for Zn−CrI_3, the 12 outermost electrons of Zn atom fill all of the 3d and 4s orbitals, leading to the zero magnetic moment of Zn; thus, M_{total} mainly stems from Cr atoms. Furthermore, the change in the M_{total} trend can also be understood from the spin polarization of TM−CrI_3 in the total density of states (TDOS), as shown in Figure 5. For example, the spin-polarization asymmetry of Sc−CrI_3 is weaker than that of Ti−CrI_3 (Figure 5a,b), thus M_{total} of Ti−CrI_3 is larger. Similarly, Co−CrI_3 has a larger spin polarization relative to Ni−CrI_3 (Figure 5c,d), leading to a larger value of M_{total}. The M_{total} values of Sc−, Mn−, Fe−, and Cu−CrI_3 calculated by the PBE + U method without and with SOC are nearly the same as those obtained by the PBE method (Table S3), indicating that the magnetic moments are not much influenced by the on-site Coulombic interaction of localized electrons and the SOC effect.

We further explore the impact of TM atoms on the FM stability of a CrI_3 monolayer. The energy difference between the Néel-AFM and FM states (E_{ex} = E(Néel-AFM) − E(FM)) in TM−CrI_3 is presented in Figure 6a. Clearly, upon the TM atom adsorption on the CrI_3 monolayer, the energy difference can be significantly increased. Specifically, the energy difference (except Co) is between 177 and 398 meV, depending on the different TM atoms. In particular, the energy difference of Sc−CrI_3 can be as high as 398 meV, which is nearly 3-fold higher than that of the pristine CrI_3 monolayer (143 meV). These results indicate that the adsorption of TM atoms (except Co) can improve the FM stability of CrI_3 monolayers.

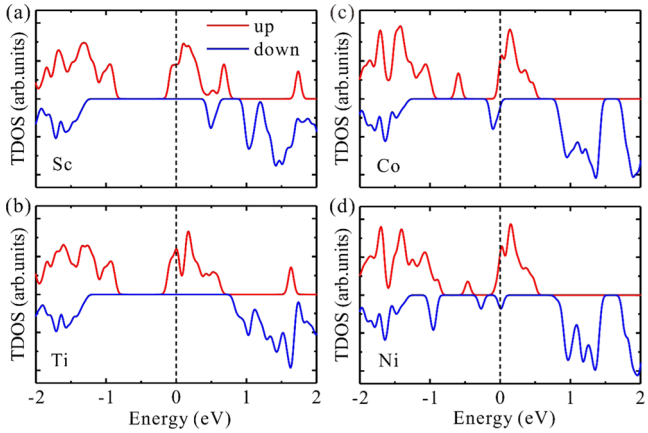

Figure 5. TDOS of (a) Sc−CrI_3, (b) Ti−CrI_3, (c) Co−CrI_3, and (d) Ni−CrI_3. The Fermi level is set at zero, denoted by the black dashed lines. The red and blue solid lines represent spin-up and spin-down channels, respectively.

To directly evaluate the stability of FM coupling, we further investigate the Curie temperature T_c of TM−CrI_3. The Heisenberg spin Hamiltonian can be written as $H = -\sum_{i,j} JS_i \cdot S_j$, where J is the nearest exchange coupling parameter and $S_{i/j}$ is the spin parallel or antiparallel to the z direction. Here, the J value can be obtained from the following formula $J = E_{ex}/24S^2$, where E_{ex} = E(Néel-AFM) − E(FM) is the exchange energy between Néel-AFM and FM states of the system. S = 3/2 was chosen as the spin of each Cr atom. The calculated J value of the pristine CrI_3 monolayer is 2.65 meV, which is in a good agreement with the previous reports.[40] We also summarized the theoretical and experimental J values for the pristine CrI_3 monolayer[30,62,63] in Table S4. The J values of TM−CrI_3 are also listed in Table S5. From the specific heat (C_V) of the pristine CrI_3 monolayer presented in Figure S9, T_c is estimated to be 46 K, which is consistent with the experimental value (45 K),[18] indicating the reliability of our approach. For TM−CrI_3 monolayers, the T_c values (except Co) are ranged from 59 to 131 K (Figure 6b), larger than that of the pristine CrI_3 monolayer (46 K). Among them, the adsorption of Sc, Ti, V, Cr, Mn, and Zn can enhance the T_c value by more than 100% as to the pristine CrI_3 monolayer. Notably, the enhanced T_c of the CrI_3 monolayer upon Sc adsorption can be increased by 185%.

It is known that the FM coupling in a CrI_3 monolayer can be understood within the Goodenough−Kanamori−Anderson (GKA) model,[64−67] which is governed by the competition between two exchange interactions: the direct exchange and the superexchange interaction. As shown in Figure 6c, the direct exchange interaction originates from the direct electron hopping between two Cr atoms, and it shows robust AFM coupling, sensitive to the distance (d) between the adjacent Cr atoms. The superexchange interaction is mediated by an I atom and prefers FM coupling, which is governed by the Cr−I−Cr bond angle (θ). To understand the enhanced FM stability of the CrI_3 monolayer upon TM atom adsorption, we give the distance (d) between the adjacent Cr atoms and the

https://doi.org/10.1021/acsami.1c01701
ACS Appl. Mater. Interfaces 2021, 13, 21593−21601

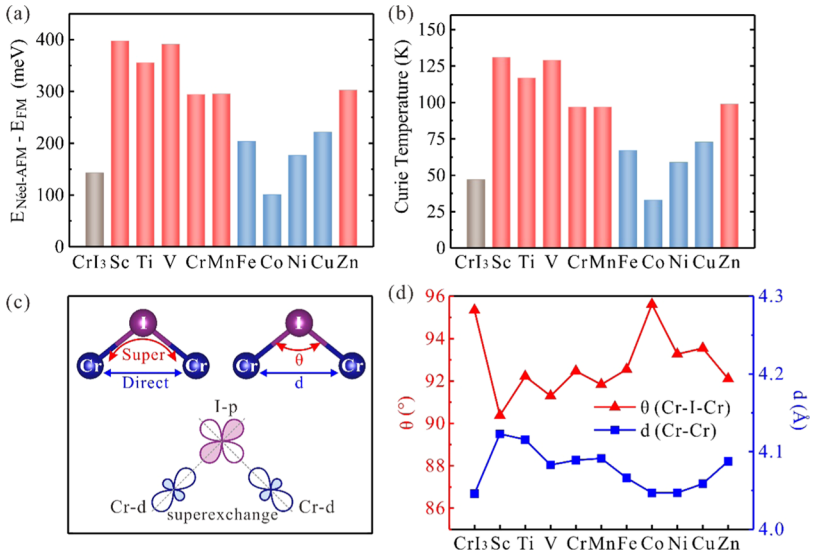

Figure 6. (a) Energy difference between the Néel-AFM and FM coupling and (b) Curie temperature of the CrI_3 monolayer with different TM atoms. (c) Schematic mechanism of direct exchange and superexchange interactions. (d) Cr−Cr distance and the Cr−I−Cr bond angle in the CrI_3 monolayer with different TM atoms.

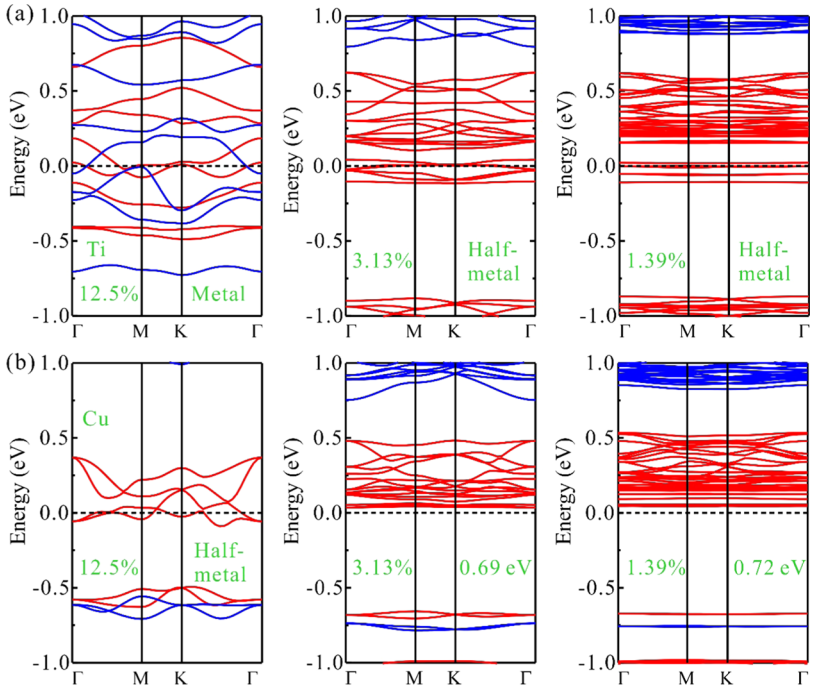

Figure 7. Spin-polarized band structures with different adatom concentrations of (a) Ti−CrI_3 and (b) Cu−CrI_3. The red and blue solid lines indicate spin-up and spin-down channels, respectively.

Cr−I−Cr bond angle (θ) in TM−CrI_3, as shown in Figure 6d. For the adsorption of Sc, Ti, V, Cr, Mn, and Zn atoms, the angles (θ) are closer to 90° than that of Fe, Co, Ni, and Cu adsorption. Thus, the superexchange interaction of the former is stronger than that for the latter, resulting in stronger FM coupling. On the other hand, due to larger distances (d) in Sc, Ti, V, Cr, Mn, and Zn−CrI_3, the AFM coupling originating from the direct exchange is weaker than that of Fe, Co, Ni, and Cu−CrI_3. Consequently, the FM stability in Sc, Ti, V, Cr, Mn, and Zn−CrI_3 is significantly enhanced. Especially for Co adsorption, the distance (d) remains almost unchanged, while the angle (θ) is slightly increased than that of the pristine CrI_3 monolayer, which leads to the weaker superexchange. As a result, the FM stability of the system with Co adatoms is lower as compared to the pristine CrI_3 monolayer.

Furthermore, taking Ti−CrI_3 and Cu−CrI_3 as examples, we investigated the effect of the TM adatom concentration on the electronic and magnetic properties of TM−CrI_3. TM−CrI_3 with the different adatom concentrations can be constructed by choosing 1 × 1 × 1, 2 × 2 × 1, and 3 × 3 × 1 CrI_3 supercells with a TM atom adsorbed, corresponding to the concentrations of 12.5, 3.13, and 1.39%, respectively. The band structures of TM−CrI_3 with different adatom concentrations are shown in Figure 7. It can be seen that Ti−CrI_3 and Cu−CrI_3 present metal and half-metal behaviors at a higher concentration of 12.5%. At a lower concentration (3.13 and

https://doi.org/10.1021/acsami.1c01701
ACS Appl. Mater. Interfaces 2021, 13, 21593−21601

1.39%), Ti−CrI_3 and Cu−CrI_3 exhibit half-metal and semiconductor characters, respectively. In addition, it is found that the T_c values of Ti−CrI_3 and Cu−CrI_3 can be increased with the increase of adatom concentration, as shown in Figure S10. Specifically, the T_c values of Ti−CrI_3 (Cu−CrI_3) are 226, 116, and 91 K (136, 71, and 61 K), respectively, corresponding to the concentrations of 12.5, 3.13, and 1.39%. The results demonstrate that the electronic structure and FM stability of TM−CrI_3 are dependent on the adatom concentration.

CONCLUSIONS

In conclusion, we carried out systematic DFT calculations to study the electronic and magnetic properties of CrI_3 with various TM atoms adsorbed on its surface. Our results show that TM−CrI_3 system can possess various electronic properties. In particular, the CrI_3 monolayer with Cu adsorption remains a semiconductor with a reduced band gap of 0.69 eV, while adsorption of other 3d TM atoms leads to a semiconductor-to-metal/half-metal/spin gapless semiconductor transition. In addition, it is found that TM atom adsorption can significantly enhance the FM stability of CrI_3 monolayers, which is related to the interplay between direct exchange and superexchange interactions. Especially, T_c for Sc−CrI_3 and V-CrI_3 can be increased by nearly a factor of three as compared to the pristine CrI_3 monolayer. The deposition of TM atoms can be done after the synthesis of the material at moderate temperatures to ensure formation of adatoms in equivalent positions but avoiding their coalescence, similar to the deposition of TMs on transition- metal dichalcogenides.[9,68] This work suggests a practical route not only to tailor the electronic properties of CrI_3 monolayers but also to improve their FM stability. We strongly believe that this strategy can be experimentally realized in the very near future, which can greatly promote the applications of CrI_3 in nanoelectronic and spintronic devices.

ASSOCIATED CONTENT

Supporting Information

The Supporting Information is available free of charge at https://pubs.acs.org/doi/10.1021/acsami.1c01701.

Four magnetic configurations and lattice constant for the CrI_3 monolayer; spin-density distributions, band structures, and the exchange coupling parameter for the CrI_3 monolayer and TM−CrI_3; and formation energy, DFT-MD simulations, and total magnetic moment for TM−CrI_3 (PDF)

AUTHOR INFORMATION

Corresponding Author

Xiaohui Hu − *College of Materials Science and Engineering, Nanjing Tech University, Nanjing 211816, China; Jiangsu Collaborative Innovation Center for Advanced Inorganic Function Composites, Nanjing Tech University, Nanjing 211816, China;* orcid.org/0000-0001-6346-1419; Email: xiaohui.hu@njtech.edu.cn

Authors

Qiang Yang − *College of Materials Science and Engineering, Nanjing Tech University, Nanjing 211816, China*

Xiaodong Shen − *College of Materials Science and Engineering, Nanjing Tech University, Nanjing 211816, China; Jiangsu Collaborative Innovation Center for Advanced Inorganic Function Composites, Nanjing Tech University, Nanjing 211816, China;* orcid.org/0000-0002-6741-0667

Arkady V. Krasheninnikov − *Institute of Ion Beam Physics and Materials Research, Helmholtz-Zentrum Dresden-Rossendorf, 01314 Dresden, Germany; Department of Applied Physics, Aalto University School of Science, 00076 Aalto, Finland;* orcid.org/0000-0003-0074-7588

Zhongfang Chen − *Department of Chemistry, University of Puerto Rico, San Juan 00931, Puerto Rico;* orcid.org/0000-0002-1445-9184

Litao Sun − *SEU-FEI Nano-Pico Center, Key Laboratory of MEMS of Ministry of Education, Collaborative Innovation Center for Micro/Nano Fabrication, Device and System, Southeast University, Nanjing 210096, China;* orcid.org/0000-0002-2750-5004

Complete contact information is available at: https://pubs.acs.org/10.1021/acsami.1c01701

Notes

The authors declare no competing financial interest.

ACKNOWLEDGMENTS

This work was supported in China by the National Natural Science Foundation of China (No. 11604047), the Natural Science Foundation of Jiangsu Province (No. BK20160694), the Jiangsu Planned Projects for Postdoctoral Research Funds (No. 2019K010A), the Priority Academic Program Development of Jiangsu Higher Education Institutions (PAPD), the Postgraduate Research and Practice Innovation Program of Jiangsu Province (KYCX20_1065), the Fundamental Research Funds for the Central Universities, and the open research fund of Key Laboratory of MEMS of Ministry of Education, Southeast University, and in USA by NASA (Grant Number 80NSSC19M0236) and NSF Center for the Advancement of Wearable Technologies (Grant 1849243). A.V.K. acknowledges funding from the German Research Foundation (DFG), Project KR 48661/2. The authors are thankful for the computational resources from the High Performance Computing Center of Nanjing Tech University, National Supercomputer Center in Tianjin.

REFERENCES

(1) Castro Neto, A. H.; Guinea, F.; Peres, N. M. R.; Novoselov, K. S.; Geim, A. K. The Electronic Properties of Graphene. *Rev. Mod. Phys.* **2009**, *81*, No. 109.

(2) Hu, X.; Björkman, T.; Lipsanen, H.; Sun, L.; Krasheninnikov, A. V. Solubility of Boron, Carbon, and Nitrogen in Transition Metals: Getting Insight into Trends from First-Principles Calculations. *J. Phys. Chem. Lett.* **2015**, *6*, 3263−3268.

(3) Heine, T. Transition Metal Chalcogenides: Ultrathin Inorganic Materials with Tunable Electronic Properties. *Acc. Chem. Res.* **2015**, *48*, 65−72.

(4) Duan, X. D.; Wang, C.; Pan, A. L.; Yu, R. Q.; Duan, X. F. Two-Dimensional Transition Metal Dichalcogenides as Atomically Thin Semiconductors: Opportunities and Challenges. *Chem. Soc. Rev.* **2015**, *44*, 8859−8876.

(5) Hu, X.; Wang, Y.; Shen, X.; Krasheninnikov, A. V.; Sun, L.; Chen, Z. 1T Phase as an Efficient Hole Injection Layer to TMDs Transistors: A Universal Approach to Achieve P-Type Contacts. *2D Mater.* **2018**, *5*, No. 031012.

(6) Kou, L.; Ma, Y.; Sun, Z.; Heine, T.; Chen, C. Two-Dimensional Topological Insulators: Progress and Prospects. *J. Phys. Chem. Lett.* **2017**, *8*, 1905−1919.

(7) Liu, L.; Kou, L.; Wang, Y.; Lu, C.; Hu, X. Electronic and Effective Mass Modulation in 2D BCN by Strain Engineering. *Nanotechnology* **2020**, *31*, No. 455702.
(8) Miró, P.; Audiffred, M.; Heine, T. An Atlas of Two-Dimensional Materials. *Chem. Soc. Rev.* **2014**, *43*, 6537−6554.
(9) Coelho, P. M.; Komsa, H. P.; Lasek, K.; Kalappattil, V.; Karthikeyan, J.; Phan, M. H.; Krasheninnikov, A. V.; Batzill, M. Room-Temperature Ferromagnetism in $MoTe_2$ by Post-Growth Incorporation of Vanadium Impurities. *Adv. Electron. Mater.* **2019**, *5*, No. 1900044.
(10) Karthikeyan, J.; Komsa, H. P.; Batzill, M.; Krasheninnikov, A. V. Which Transition Metal Atoms can be Embedded into Two-Dimensional Molybdenum Dichalcogenides and Add Magnetism? *Nano Lett.* **2019**, *19*, 4581−4587.
(11) Yang, Q.; Kou, L.; Hu, X.; Wang, Y.; Lu, C.; Krasheninnikov, A. V.; Sun, L. Strain Robust Spin Gapless Semiconductors/Half-Metals in Transition Metal Embedded MoSe2 Monolayer. *J. Phys.: Condens. Matter* **2020**, *32*, No. 365305.
(12) Yazyev, O. V.; Helm, L. Defect-Induced Magnetism in Graphene. *Phys. Rev. B* **2007**, *75*, No. 125408.
(13) Kou, L.; Tang, C.; Guo, W.; Chen, C. Tunable Magnetism in Strained Graphene with Topological Line Defect. *ACS Nano* **2011**, *5*, 1012−1017.
(14) Avsar, A.; Cheon, C. Y.; Pizzochero, M.; Tripathi, M.; Ciarrocchi, A.; Yazyev, O. V.; Kis, A. Probing Magnetism in Atomically Thin Semiconducting $PtSe_2$. *Nat. Commun.* **2020**, *11*, No. 4806.
(15) Ma, Y.; Dai, Y.; Guo, M.; Niu, C.; Yu, L.; Huang, B. Strain-Induced Magnetic Transitions in Half-Fluorinated Single Layers of BN, GaN and Graphene. *Nanoscale* **2011**, *3*, 2301.
(16) Ma, Y.; Dai, Y.; Guo, M.; Niu, C.; Zhu, Y.; Huang, B. Evidence of the Existence of Magnetism in Pristine VX_2 Monolayers (X = S, Se) and Their Strain-Induced Tunable Magnetic Properties. *ACS Nano* **2012**, *6*, 1695−1701.
(17) Lee, C.; Katmis, F.; Jarillo-Herrero, P.; Moodera, J. S.; Gedik, N. Direct Measurement of Proximity-Induced Magnetism at the Interface between a Topological Insulator and a Ferromagnet. *Nat. Commun.* **2016**, *7*, No. 12014.
(18) Huang, B.; Clark, G.; Navarro-Moratalla, E.; Klein, D. R.; Cheng, R.; Seyler, K. L.; Zhong, D.; Schmidgall, E.; McGuire, M. A.; Cobden, D. H.; Yao, W.; Xiao, D.; Jarillo-Herrero, P.; Xu, X. Layer-Dependent Ferromagnetism in a van der Waals Crystal Down to the Monolayer Limit. *Nature* **2017**, *546*, 270−273.
(19) Gong, C.; Li, L.; Li, Z.; Ji, H.; Stern, A.; Xia, Y.; Cao, T.; Bao, W.; Wang, C.; Wang, Y.; Qiu, Z. Q.; Cava, R. J.; Louie, S. G.; Xia, J.; Zhang, X. Discovery of Intrinsic Ferromagnetism in Two-Dimensional van der Waals Crystals. *Nature* **2017**, *546*, 265−269.
(20) Deng, Y.; Yu, Y.; Song, Y.; Zhang, J.; Wang, N. Z.; Sun, Z.; Yi, Y.; Wu, Y. Z.; Wu, S.; Zhu, J.; Wang, J.; Chen, X. H.; Zhang, Y. Gate-Tunable Room-Temperature Ferromagnetism in Two-Dimensional Fe_3GeTe_2. *Nature* **2018**, *563*, 94−99.
(21) Chen, W.; Sun, Z.; Wang, Z.; Gu, L.; Xu, X.; Wu, S.; Gao, C. Direct Observation of van der Waals Stacking-Dependent Interlayer Magnetism. *Science* **2019**, *366*, 983−987.
(22) Zhao, Y.; Gu, J.; Chen, Z. Oxygen Evolution Reaction on 2D Ferromagnetic Fe_3GeTe_2: Boosting the Reactivity by the Self-Reduction of Surface Hydroxyl. *Adv. Funct. Mater.* **2019**, *29*, No. 1904782.
(23) Hu, X.; Zhao, Y.; Shen, X.; Krasheninnikov, A. V.; Chen, Z.; Sun, L. Enhanced Ferromagnetism and Tunable Magnetism in Fe_3GeTe_2 Monolayer by Strain Engineering. *ACS Appl. Mater. Interfaces* **2020**, *12*, 26367−26373.
(24) Ma, A. N.; Wang, P. J.; Zhang, C. W. Intrinsic Ferromagnetism with High Temperature, Strong Anisotropy and Controllable Magnetization in the CrX (X = P, As) Monolayer. *Nanoscale* **2020**, *12*, 5464−5470.
(25) Wang, B.; Zhang, X.; Zhang, Y.; Yuan, S.; Guo, Y.; Dong, S.; Wang, J. Prediction of a Two-Dimensional High-Tc f-Electron Ferromagnetic Semiconductor. *Mater. Horiz.* **2020**, *7*, 1623−1630.
(26) Tang, C.; Ostrikov, K. K.; Sanvito, S.; Du, A. Prediction of Room-Temperature Ferromagnetism and Large Perpendicular Magnetic Anisotropy in a Planar Hypercoordinate FeB_3 Monolayer. *Nanoscale Horiz.* **2021**, *6*, 43−48.
(27) Jiang, P.; Li, L.; Liao, Z.; Zhao, Y. X.; Zhong, Z. Spin Direction-Controlled Electronic Band Structure in Two-Dimensional Ferromagnetic CrI_3. *Nano Lett.* **2018**, *18*, 3844−3849.
(28) Webster, L.; Liang, L.; Yan, J. A. Distinct Spin-Lattice and Spin-Phonon Interactions in Monolayer Magnetic CrI_3. *Phys. Chem. Chem. Phys.* **2018**, *20*, 23546−23555.
(29) Chen, L.; Chung, J.-H.; Gao, B.; Chen, T.; Stone, M. B.; Kolesnikov, A. I.; Huang, Q.; Dai, P. Topological Spin Excitations in Honeycomb Ferromagnet CrI_3. *Phys. Rev. X* **2018**, *8*, No. 041028.
(30) Wu, M.; Li, Z.; Cao, T.; Louie, S. G. Physical Origin of Giant Excitonic and Magneto-Optical Responses in Two-Dimensional Ferromagnetic Insulators. *Nat. Commun.* **2019**, *10*, No. 2371.
(31) Cenker, J.; Huang, B.; Suri, N.; Thijssen, P.; Miller, A.; Song, T.; Taniguchi, T.; Watanabe, K.; McGuire, M. A.; Xiao, D.; Xu, X. Direct Observation of Two-Dimensional Magnons in Atomically Thin CrI_3. *Nat. Phys.* **2021**, *17*, 20−25.
(32) Soriano, D.; Katsnelson, M. I.; Fernandez-Rossier, J. Magnetic Two-Dimensional Chromium Trihalides: A Theoretical Perspective. *Nano Lett.* **2020**, *20*, 6225−6234.
(33) Jiang, S.; Li, L.; Wang, Z.; Mak, K. F.; Shan, J. Controlling Magnetism in 2D CrI_3 by Electrostatic Doping. *Nat. Nanotechnol.* **2018**, *13*, 549−553.
(34) Tang, C.; Zhang, L.; Du, A. Tunable Magnetic Anisotropy in 2D Magnets Via Molecular Adsorption. *J. Mater. Chem. C* **2020**, *8*, 14948−14953.
(35) Huang, B.; Clark, G.; Klein, D. R.; MacNeill, D.; Navarro-Moratalla, E.; Seyler, K. L.; Wilson, N.; McGuire, M. A.; Cobden, D. H.; Xiao, D.; Yao, W.; Jarillo-Herrero, P.; Xu, X. Electrical Control of 2D Magnetism in Bilayer CrI_3. *Nat. Nanotechnol.* **2018**, *13*, 544−548.
(36) Zhao, Y.; Lin, L.; Zhou, Q.; Li, Y.; Yuan, S.; Chen, Q.; Dong, S.; Wang, J. Surface Vacancy-Induced Switchable Electric Polarization and Enhanced Ferromagnetism in Monolayer Metal Trihalides. *Nano Lett.* **2018**, *18*, 2943−2949.
(37) Pizzochero, M. Atomic-Scale Defects in the Two-Dimensional Ferromagnet CrI_3 from First Principles. *J. Phys. D: Appl. Phys.* **2020**, *53*, No. 244003.
(38) Pizzochero, M.; Yazyev, O. V. Inducing Magnetic Phase Transitions in Monolayer CrI_3 Via Lattice Deformations. *J. Phys. Chem. C* **2020**, *124*, 7585−7590.
(39) Shang, J.; Tang, X.; Tan, X.; Du, A.; Liao, T.; Smith, S. C.; Gu, Y.; Li, C.; Kou, L. Stacking-Dependent Interlayer Magnetic Coupling in 2D $CrI_3/CrGeTe_3$ Nanostructures for Spintronics. *ACS Appl. Nano Mater.* **2020**, *3*, 1282−1288.
(40) Webster, L.; Yan, J.-A. Strain-Tunable Magnetic Anisotropy in Monolayer $CrCl_3$, $CrBr_3$, and CrI_3. *Phys. Rev. B* **2018**, *98*, No. 144411.
(41) Krasheninnikov, A. V.; Lehtinen, P. O.; Foster, A. S.; Pyykko, P.; Nieminen, R. M. Embedding Transition-Metal Atoms in Graphene: Structure, Bonding, and Magnetism. *Phys. Rev. Lett.* **2009**, *102*, No. 126807.
(42) Hu, X.; Zhang, W.; Sun, L.; Krasheninnikov, A. V. Gold-Embedded Zigzag Graphene Nanoribbons as Spin Gapless Semiconductors. *Phys. Rev. B* **2012**, *86*, No. 195418.
(43) Hu, X.; Wan, N.; Sun, L.; Krasheninnikov, A. V. Semiconductor to Metal to Half-Metal Transition in Pt-Embedded Zigzag Graphene Nanoribbons. *J. Phys. Chem. C* **2014**, *118*, 16133−16139.
(44) Wang, J.; Sun, F.; Yang, S.; Li, Y.; Zhao, C.; Xu, M.; Zhang, Y.; Zeng, H. Robust Ferromagnetism in Mn-Doped MoS_2 Nanostructures. *Appl. Phys. Lett.* **2016**, *109*, No. 092401.
(45) Kochat, V.; Apte, A.; Hachtel, J. A.; Kumazoe, H.; Krishnamoorthy, A.; Susarla, S.; Idrobo, J. C.; Shimojo, F.; Vashishta, P.; Kalia, R.; Nakano, A.; Tiwary, C. S.; Ajayan, P. M. Re Doping in 2D Transition Metal Dichalcogenides as a New Route to Tailor Structural Phases and Induced Magnetism. *Adv. Mater.* **2017**, *29*, No. 1703754.

https://doi.org/10.1021/acsami.1c01701
ACS Appl. Mater. Interfaces 2021, 13, 21593−21601

(46) Zhang, Q.; Ren, Z.; Wu, N.; Wang, W.; Gao, Y.; Zhang, Q.; Shi, J.; Zhuang, L.; Sun, X.; Fu, L. Nitrogen-Doping Induces Tunable Magnetism in ReS_2. *npj 2D Mater. Appl.* **2018**, *2*, No. 22.
(47) Song, C.; Xiao, W.; Li, L.; Lu, Y.; Jiang, P.; Li, C.; Chen, A.; Zhong, Z. Tunable Band Gap and Enhanced Ferromagnetism by Surface Adsorption in Monolayer $Cr_2Ge_2Te_6$. *Phys. Rev. B* **2019**, *99*, No. 214435.
(48) Guo, Y.; Yuan, S.; Wang, B.; Shi, L.; Wang, J. Half-Metallicity and Enhanced Ferromagnetism in Li-Adsorbed Ultrathin Chromium Triiodide. *J. Mater. Chem. C* **2018**, *6*, 5716−5720.
(49) Blöchl, P. E. Projector Augmented-Wave Method. *Phys. Rev. B* **1994**, *50*, No. 17953.
(50) Kresse, G.; Joubert, D. From Ultrasoft Pseudopotentials to the Projector Augmented-Wave Method. *Phys. Rev. B* **1999**, *59*, No. 1758.
(51) Kresse, G.; Furthmuller, J. Efficient Iterative Schemes for Ab Initio Total-Energy Calculations Using a Plane-Wave Basis Set. *Phys. Rev. B* **1996**, *54*, No. 11169.
(52) Kresse, G.; Furthmuller, J. Efficiency of Ab-Initio Total Energy Calculations for Metals and Semiconductors Using a Plane-Wave Basis Set. *Comput. Mater. Sci.* **1996**, *6*, 15−50.
(53) Perdew, J. P.; Burke, K.; Ernzerhof, M. Generalized Gradient Approximation Made Simple. *Phys. Rev. Lett.* **1996**, *77*, No. 3865.
(54) Tang, C.; Zhang, L.; Sanvito, S.; Du, A. Electric-Controlled Half-Metallicity in Magnetic Van Der Waals Heterobilayer. *J. Mater. Chem. C* **2020**, *8*, 7034−7040.
(55) Chen, S.; Huang, C.; Sun, H.; Ding, J.; Jena, P.; Kan, E. Boosting the Curie Temperature of Two-Dimensional Semiconducting CrI_3 Monolayer through Van Der Waals Heterostructures. *J. Phys. Chem. C* **2019**, *123*, 17987−17993.
(56) Liu, M.; Chen, Q.; Huang, Y.; Cao, C.; He, Y. A First-Principles Study of Transition Metal Doped Arsenene. *Superlattices Microstruct.* **2016**, *100*, 131−141.
(57) Heyd, J.; Scuseria, G. E.; Ernzerhof, M. Hybrid Functionals Based on a Screened Coulomb Potential. *J. Chem. Phys.* **2003**, *118*, 8207−8215.
(58) Zhao, Y.; Zhang, J. J.; Yuan, S.; Chen, Z. Nonvolatile Electrical Control and Heterointerface-Induced Half-Metallicity of 2D Ferromagnets. *Adv. Funct. Mater.* **2019**, *29*, No. 1901420.
(59) Dillon, J. F.; Olson, C. E. Magnetization, Resonance, and Optical Properties of the Ferromagnet CrI_3. *J. Appl. Phys.* **1965**, *36*, 1259−1260.
(60) Wang, X. L. Proposal for a New Class of Materials: Spin Gapless Semiconductors. *Phys. Rev. Lett.* **2008**, *100*, No. 156404.
(61) Sui, X.; Si, C.; Shao, B.; Zou, X.; Wu, J.; Gu, B.-L.; Duan, W. Tunable Magnetism in Transition-Metal-Decorated Phosphorene. *J. Phys. Chem. C* **2015**, *119*, 10059−10063.
(62) Xu, C.; Feng, J.; Xiang, H.; Bellaiche, L. Interplay between Kitaev Interaction and Single Ion Anisotropy in Ferromagnetic CrI_3 and $CrGeTe_3$ Monolayers. *npj Comput. Mater.* **2018**, *4*, No. 57.
(63) Pizzochero, M.; Yadav, R.; Yazyev, O. V. Magnetic Exchange Interactions in Monolayer CrI_3 from Many-Body Wavefunction Calculations. *2D Mater.* **2020**, *7*, No. 035005.
(64) Goodenough, J. B. Theory of the Role of Covalence in the Perovskite-Type Manganites [La,M(II)]MnO_3. *Phys. Rev.* **1955**, *100*, No. 564.
(65) Kanamori, J. Crystal Distortion in Magnetic Compounds. *J. Appl. Phys.* **1960**, *31*, S14−S23.
(66) Anderson, P. W. New Approach to the Theory of Superexchange Interactions. *Phys. Rev.* **1959**, *115*, No. 2.
(67) Tang, X.; Sun, W.; Gu, Y.; Lu, C.; Kou, L.; Chen, C. CoB_6 Monolayer: A Robust Two-Dimensional Ferromagnet. *Phys. Rev. B* **2019**, *99*, No. 045445.
(68) Coelho, P. M.; Komsa, H. P.; Coy Diaz, H.; Ma, Y.; Krasheninnikov, A. V.; Batzill, M. Post-Synthesis Modifications of Two-Dimensional $MoSe_2$ or $MoTe_2$ by Incorporation of Excess Metal Atoms into the Crystal Structure. *ACS Nano* **2018**, *12*, 3975−3984.

https://doi.org/10.1021/acsami.1c01701
ACS Appl. Mater. Interfaces 2021, 13, 21593−21601